Available online at www.sciencedirect.com
SCIENCE DIRECT®
Thermochimica Acta 403 (2003) 129–136
thermochimica acta
www.elsevier.com/locate/tca

High-temperature high-pressure crystallization and sintering behavior of brookite-free nanostructured titanium dioxide: in situ experiments using synchrotron radiation

R. Nicula*, M. Stir, C. Schick, E. Burkel

Universität Rostock, FB Physik, August-Bebel-Str. 55, D-18051 Rostock, Germany

Received 16 October 2002; received in revised form 1 March 2003; accepted 3 March 2003

Abstract

The formation, stability and physico-chemical properties of TiO_2 powders are strongly influenced by the actual synthesis and processing routes employed. Pure and metal-doped nanostructured TiO_2 samples were obtained using the sol–gel method. In situ X-ray diffraction (XRD) experiments using synchrotron radiation were performed to explore the high-temperature/high-pressure stability and sintering behavior of these nanomaterials. The present results show a strong decrease of the anatase-to-rutile transition temperatures with increasing applied pressure, thus opening new perspectives for the development of efficient low-temperature sintering procedures.

Keywords: Nanomaterials; Sol–gel synthesis; Phase transitions

1. Introduction

Nanostructured materials were proven to exhibit unique mechanical, chemical, electrical, optical and magnetic properties [1]. Pure and metal-doped nanostructured titanium oxide materials are essential for the development of advanced electrochemical solar cells [2], photocatalytic devices [3] as well as optical and electron-sensitive coatings [4].

An important issue in the development and use of nanomaterials in everyday applications is their ability to maintain ultra-fine particle sizes within extended temperature–pressure ranges. The surface free energy and the surface stress govern the thermodynamic phase stability for ultra-fine-grained materials [5]. Both parameters may be tuned with sufficient accuracy by intentionally modifying the surface chemistry of the nanosized particles and by external applied pressure, respectively.

The formation, stability and physico-chemical properties of nanostructured TiO_2 powders are determined by the details of the actual synthesis and processing routes employed. Pure and metal-doped nanostructured TiO_2 samples were obtained using the sol–gel method. In situ X-ray diffraction (XRD) experiments using synchrotron radiation were performed to observe the high-temperature/high-pressure stability and sintering behavior of these nanomaterials. The present results show a strong decrease of the anatase-to-rutile transition temperatures with increasing applied pressure. Efficient transformation-assisted low-temperature sintering procedures [6–10] may

* Corresponding author. Tel.: +49-381-4981725; fax: +49-381-4981726.
E-mail address: nicula@physik1.uni-rostock.de (R. Nicula).

0040-6031/03/$ – see front matter © 2003 Elsevier Science B.V. All rights reserved.
doi:10.1016/S0040-6031(03)00158-8

therefore be developed to produce large-volume nanostructured ceramic parts with improved properties and mechanical resistance.

2. Experimental

2.1. Sol–gel synthesis

Pure and Ag-doped titanium oxide samples were obtained following a sol–gel procedure using tetra-isopropylorthotitanate (TPOT) and titanium tetra-isopropoxide (TTIP) as precursor materials. Under vigorous stirring, TTIP was added to a water–ethanol mixture. The solution was further mixed in an ultrasonic bath, then aged at room temperature in air for 24 h. This procedure resulted in centimeter sized transparent, gel bulk monoliths. A similar procedure was followed for the Ag-doped samples. After the hydrolysis of TTIP, $AgNO_3$ was added as a precursor for the silver ions. The resulting sols were then air dried at room temperature for a few days.

2.2. In situ X-ray diffraction experiments using synchrotron radiation

The crystallization sequence and sintering behavior of the as-prepared brookite-free samples was followed for temperatures as high as 850 °C. The in situ experiments were performed at the high-resolution powder diffractometer at the B2 HASYLAB/DESY beamline in Hamburg, Germany. We used a capillary sample holder and a STOE furnace/oven. The specimen temperature was measured using thermocouples mounted in the immediate vicinity of the capillary sample holder. The scattered intensity was monitored using a semi-circular image-plate detector, which allows the one-step acquisition of high-resolution XRD patterns. The instrumental resolution function $\beta_g(2\theta)$ was determined using NIST Al_2O_3 and LaB_6 standards. The data-acquisition time was optimized to about 20 min per scattering pattern. For each of the sol–gel derived samples, about 50 diffraction patterns were collected at temperatures between 100 and 850 °C. The synchrotron radiation wavelength was equal to $\lambda = 0.11196$ nm.

The in situ high-temperature synchrotron radiation diffraction experiments under high-pressure were performed in energy-dispersive mode using the MAX80 multiple-anvil high-pressure facility (beamline F2.1, HASYLAB). The powder samples were loaded into 6 or 8 mm boron cubes. A boron nitride (BN) cylinder together with BN powder added above and below the specimen provide a highly-stable, chemically-inert environment for the sample material. Pressure is calibrated using NaCl as reference standard. Several heating experiments (up to 1300 °C) were performed at different applied pressures (up to 2.5 GPa) for each sample. The typical data-acquisition time per diffraction pattern ranged from 3 to 10 min.

2.3. Thermogravimetry (TG) and differential scanning calorimetry (DSC)

The thermal stability of the sol–gel-derived samples was investigated by TG and DSC, using a SETARAM LABSYS TG–DSC instrument. The samples were first vacuum dried at 90 °C for 3 h, then TG–DSC measurements were simultaneously performed up 700 °C at a heating rate of 2 °C/min.

2.4. X-ray diffraction data-analysis procedure

For the analysis of angular-dispersive diffraction patterns, we used the software package PeakFit [11]. The experimental scattering patterns were modeled by assuming a polynomial baseline and Voigt-type individual diffraction lines. The modified Voigt function used for the present peak-shape analysis provides the Gauss (ω_G) and Cauchy–Lorentz (ω_L) components of the linewidth as fitting variables:

$$\begin{aligned}\mathrm{Voigt}(2\theta) &= a_0 \frac{\int_{-\infty}^{\infty} [\exp(-t^2)/((a_3^2/2a_2^2) + (((x-a_1)/a_2\sqrt{2}) - t)^2)]\,\mathrm{d}t}{\int_{-\infty}^{\infty} [\exp(-t^2)/((a_3^2/2a_2^2) + t^2)]\,\mathrm{d}t} \\ &= I_0 \frac{\int_{-\infty}^{\infty} [\exp(-t^2)/((\omega_L^2/2\omega_G^2) + ((2\theta - 2\theta_0)/\omega_G\sqrt{2}) - t)^2)]\,\mathrm{d}t}{\int_{-\infty}^{\infty} [\exp(-t^2)/((\omega_L^2/2\omega_G^2) + t^2)]\,\mathrm{d}t}\end{aligned} \quad (1)$$

together with the usual parameters: peak position $2\theta_0$, amplitude I_0 (the diffracted intensity at $2\theta_0$), and the full-width-half-maximum (β). The instrumental resolution function $\beta_g(2\theta)$ was first obtained from the experimental data on the standard NIST Al_2O_3 and

LaB_6 specimens, using an interpolation procedure for the angular range of interest ((10–70) × 2θ). The instrumental broadening correction was performed for the experimental FWHM values according to the equation:

$$\beta_f^2 = (\beta_h - \beta_g)\sqrt{\beta_f^2 - \beta_g^2} \quad (2)$$

where the indices h, g and f indicate the experimental (β_h), instrumental (β_g) and specimen (β_f) FWHM contributions, respectively. The values for the corrected FWHM β_f were further used to evaluate the "apparent" particle size (D) according to the Scherrer equation, assuming microstrain-free specimens and $K \approx 1$:

$$\beta_f = \frac{K\lambda}{D\cos\theta} \quad (3)$$

Additional information on the temperature evolution of average grain-sizes and root-mean-square (rms) strain ε were obtained directly from the Cauchy–Gauss components of the linewidths, within the limits of the Halder–Wagner approximation [12]. The present preliminary analysis is restricted to the strongest anatase (1 0 1) and rutile (1 1 0) reflections. The more detailed examination of line profiles based on the 'double-Voigt' method [13] which is equivalent to the Waren–Averbach procedure [14] will be described in a forthcoming paper [15].

3. Results

3.1. High-temperature X-ray diffraction (HTXRD)

For the sol–gel-derived titanium dioxide samples prepared using ethanol, the high-resolution diffraction patterns measured within the temperature range between 40 and 860 °C are illustrated in Fig. 1. The initially amorphous samples transform to nanostructured anatase at temperatures close to 100 °C. No diffraction lines corresponding to the brookite phase were observed (brookite is a minority by-product of most synthesis procedures).

The onset of the anatase-to-rutile transition is observed at $T = 460$ °C. The anatase (A) and rutile (R) phases coexist up to 780 °C. Above this temperature, only rutile diffraction lines could be noticed. The evolution of the "apparent" particle sizes and relative

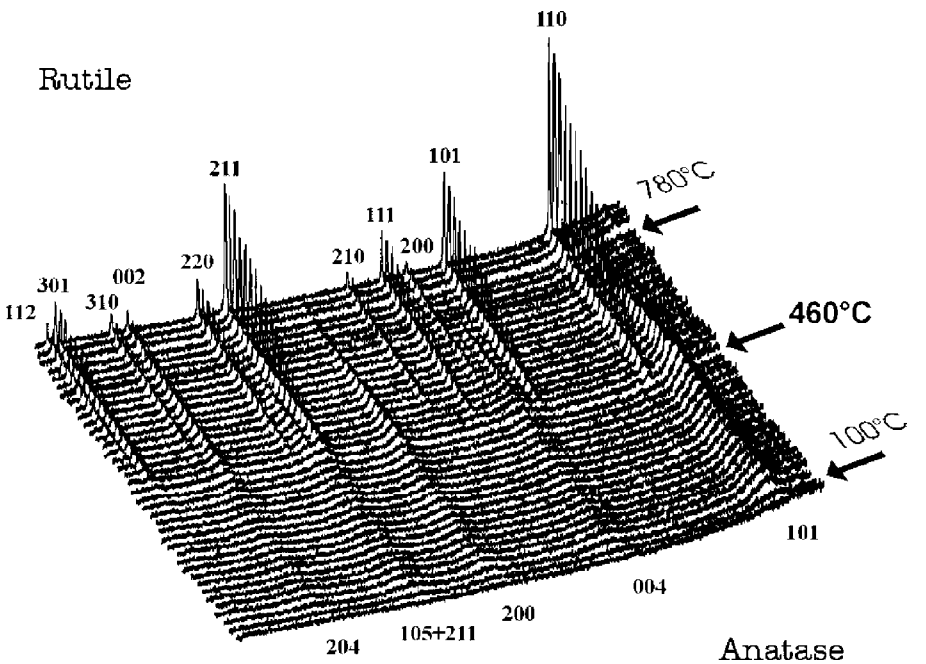

Fig. 1. High-temperature synchrotron radiation diffraction patterns of titanium dioxide sol–gel-derived powders.

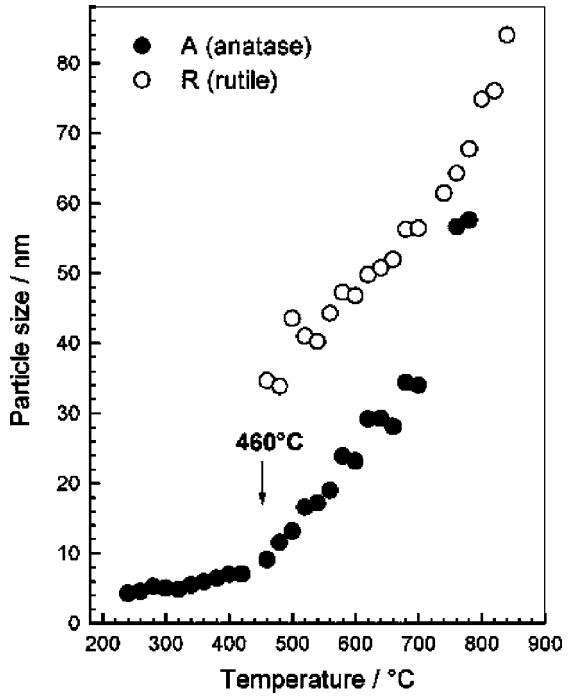

Fig. 2. The evolution of the "apparent" particle-size with temperature (based on the Scherrer equation, see Section 2).

weight fractions [5] for the anatase and rutile constituent phases against temperature are illustrated in Figs. 2 and 3, respectively.

As readily seen from Figs. 1 and 2, in the absence of secondary phases such as brookite, the crystallite size of the anatase phase remains practically unchanged to its initial value of about 5 nm, for the entire temperature range below the anatase-to-rutile (A → R) phase transition. The onset of the transition at 460 °C also triggers the faster coarsening of the anatase particles, which proceeds up to the complete transformation into rutile at 780 °C. Another important feature is that the initial rutile crystallites (of about 30 nm) are almost five times larger than the anatase particles already at the onset of the A → R transition. We also notice that the titania grain-sizes remain well below 100 nm even at temperatures close to 900 °C, which is a good premise for obtaining bulk nanostructured TiO_2 specimens with good thermal stability below 1000 °C. Finally, Fig. 3 indicates that mixed-phase samples equivalent to the Degussa P25 product (80% anatase, 20% rutile) would be obtained using ambient pressure sintering at around 500 °C, with average crystallite sizes of only 12 nm for anatase and around 30 nm for rutile.

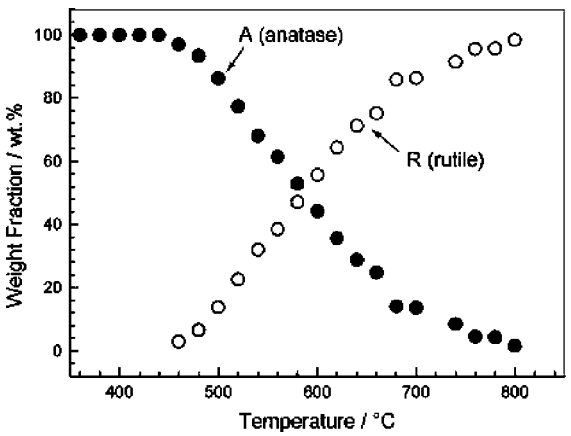

Fig. 3. The evolution of relative fractions (wt.%) of the anatase and rutile phases against temperature.

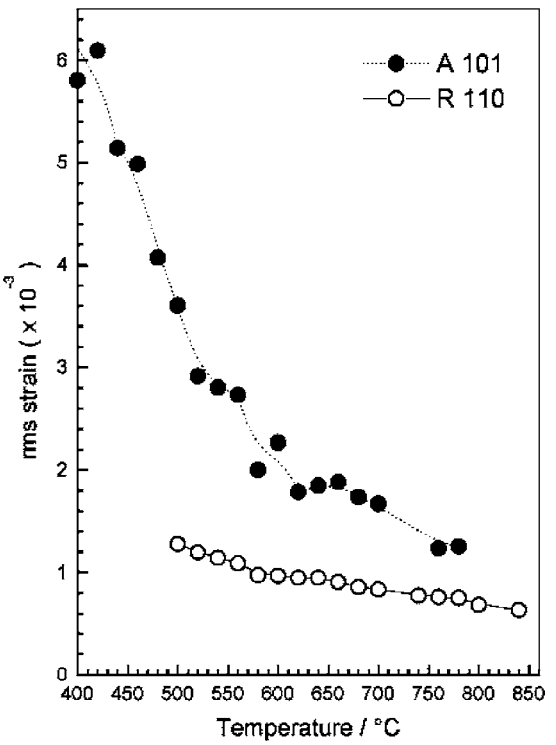

Fig. 4. Temperature evolution of the rms strain for the anatase and rutile phases.

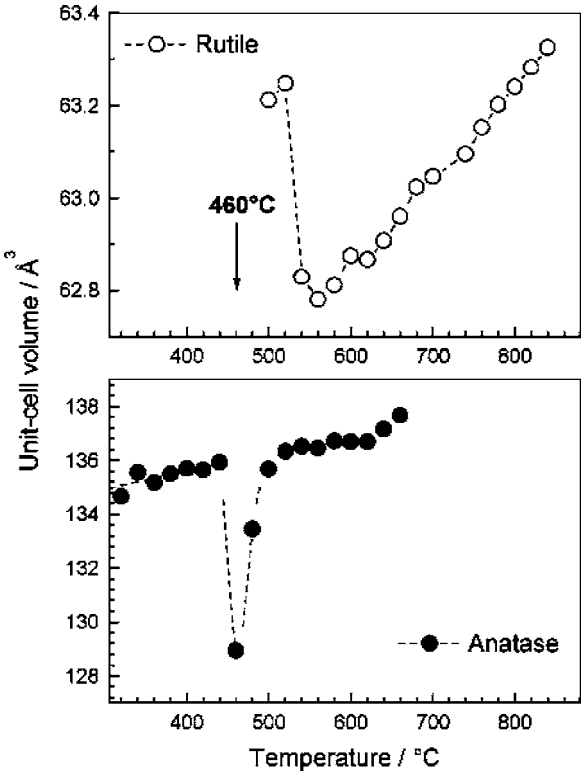

Fig. 5. Temperature evolution of the unit-cell volume for the anatase and rutile phases.

The temperature evolution of the rms strain (Fig. 4) and unit-cell volume (Fig. 5) could also be determined independently for each of the constituent crystalline phases. The anatase phase exhibits larger rms strain values than rutile over the whole temperature range. This indicates that microstrain could be one of the main causes for the instability of the nanometer-size anatase particles. The anatase rms strain decreases rapidly with increasing temperature above 400 °C (Fig. 4) which correlates with the observed increase of the apparent particle size (Fig. 2). The average strain for the rutile phase is lower (about 1×10^{-3}) and shows a less-pronounced temperature evolution, indicating that the larger rutile nanoparticles are insignificantly affected by volume and surface strain effects.

The temperature evolution of the unit-cell volume of the anatase and rutile phases is illustrated in Fig. 5. As expected, the lattice parameters are highly sensitive to the structural phase transition: the onset of the A → R transition at 460 °C is also detected by sudden changes of the unit-cell volumes of each of the constituent phases. The volume change is largely due to the change in the *c* lattice parameter, the other lattice constants being less affected (not shown). Fig. 5 demonstrates also that the onset of the A → R transition is accompanied by a 4% reduction of the volume of the anatase phase. This effect was already successfully exploited in the transformation-assisted synthesis of metal-doped titania-matrix ceramic nanocomposites [15,16]. The volume change at the onset of the A → R transition further relaxes with increasing temperature: above 560 °C, the unit-cell volume changes are due to thermal expansion only (Fig. 5).

3.2. High-pressure X-ray diffraction

Energy-dispersive X-ray diffraction spectra were collected at the MAX80 station (HASYLAB) using a diffraction angle $\theta = 3.77°$ at $p = 2.38$ kbar $\approx$ 0.24 GPa and temperatures as high as 700 °C (Fig. 6). In Fig. 6, the strong boron nitride BN (2 0 0) Bragg reflection was removed from the diffraction pattern to allow the observation of the anatase A (1 0 1) diffraction line. Under pressure, the amorphous to crystalline anatase phase transition occurs at about 130 °C. However, the onset of the A → R transition is observed at a much lower temperature, namely at only 200 °C. The anatase and rutile phases coexist over an extended temperature range: the A → R transition is completed at 600 °C. No secondary phases were formed during the sintering process. We notice that the anatase phase diffraction lines maintain a broadened profile over the entire temperature range. In contrast, the diffraction lines of the rutile phase are rather sharp, even at the onset of the A → R transition, i.e. the temperature evolution of rutile nanoparticles is very similar to the one observed under ambient pressure conditions.

3.3. Thermogravimetry–differential scanning calorimetry results

The TG–DSC results for the samples dried at 90 °C for 3 h are illustrated in Fig. 7 (initial mass of the specimen $m_p = 144$ mg, after drying $m_p = 89$ mg). The specific heat-flow (HF) signal reveals an endothermal

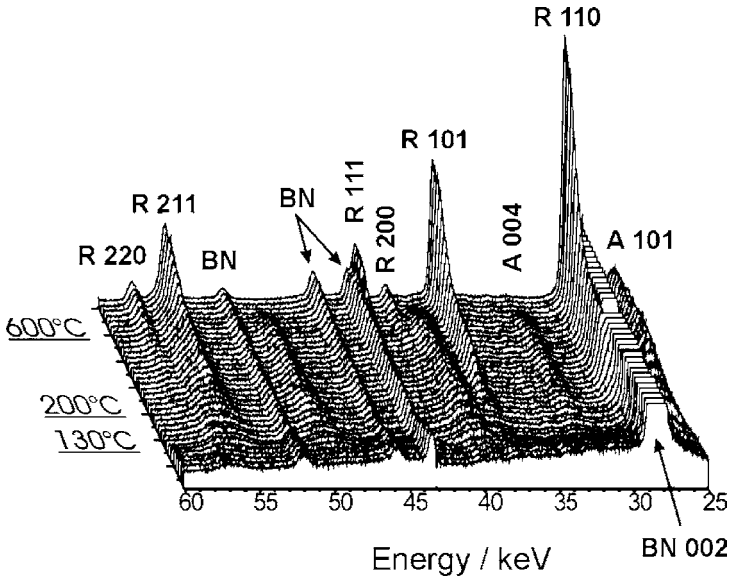

Fig. 6. Energy-dispersive X-ray diffraction (EDXRD) spectra collected at 0.238 GPa with increasing temperature (up to 700 °C). The BN (2 0 0) reflection was removed to allow the observation of the anatase A (1 0 1) diffraction line.

transition between 90 and 200 °C, which is related to the pronounced mass loss within this temperature interval. We may therefore associate this endothermal effect to the further removal of solvent material, a process not completed during the pre-heating stage. Further mass loss is observed however at a reduced rate between 220 and 360 °C, becoming insignificant for temperatures above 450 °C. The first strong exothermal maximum in the specific HF (DSC) signal at 240 °C represents the anatase crystallization

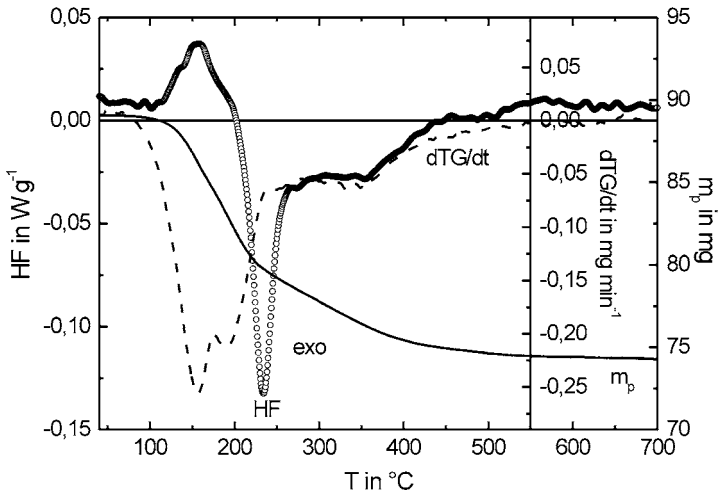

Fig. 7. Thermogravimetry (TG) and differential scanning calorimetry (DSC) results: the specific heat flow (HF) is illustrated by the open symbols curve (exothermal DSC signal downwards). The continuous black curve shows the temperature evolution of the specimen mass (m_p), while the rate of the TG signal is given by the dotted line (black).

from the amorphous precursor state. The onset temperature of the amorphous-to-anatase transition (approx. 200 °C) coincides with the change in the rate of mass loss (thermogravimetric) signal at 220 °C, indicating that solvent removal becomes substantially more difficult after the crystallization of anatase particles above 200 °C. This observation immediately suggests that at this stage only thin surface/interface layers are still trapped between the anatase nanoparticles; their removal is more difficult to achieve and the mass loss process slows down accordingly. Moreover, the growth of the anatase grains is inhibited within this temperature interval. The nucleation of rutile TiO_2 occurs progressively once the solvent removal is locally completed. This results in a broad exothermal effect centered at approx. 360 °C. Rutile nucleation thus seems to occur at the surface of anatase grains, initially leading to the formation of core–shell particles. The anatase-to-rutile transition further proceeds from the surface towards the interior of the particles, so that relatively large rutile grains result in a short time.

4. Discussion and conclusions

The use of the unique properties of nanostructured materials derived from their ultra-fine-grain size in technological applications is restricted by our ability to stabilize fine microstructures at the nanometer scale for extended temperature and pressure ranges. It was earlier recognized that the surface free energy and surface stress play a major role in the stability of nanosized particles. Both parameters can be used for tuning the phase stability of competing crystalline phases, for example by modifying the chemistry of inner surfaces/interfaces in the bulk material or by external applied pressure. Various recent studies have pointed out that the temperature–pressure phase diagrams of coarse-grained specimens are no longer valid for nanostructured materials: for example, the relative phase stability was found to be reversed due to the enhanced surface energy contribution at very fine particle sizes [5,17–20].

In situ high-temperature high-pressure X-ray diffraction experiments using synchrotron radiation are highly valuable methods in exploring the phase stability of these interface-controlled nanomaterials. These methods were here used to examine the pressure–temperature phase diagram of brookite-free titania nanosized powders prepared by the sol–gel method. For coarse-grained polycrystalline TiO_2 under ambient conditions, the rutile phase is thermodynamically stable relative to both anatase and brookite polymorphs. The onset temperature of the A → R transition for macrocrystalline TiO_2 is usually higher than 900 °C [21]. Various ambient pressure onset temperatures well below 900 °C were reported for specimens with fine-grain-sizes [5,22–24]. The spread in the values previously reported in the literature may to a certain extent be attributed to the presence or absence of minor secondary phases such as brookite, which also plays an important role in the interface stabilization of anatase [16]. For the brookite-free titania samples investigated here, the onset temperature for the A → R transition equals 460 °C, which is roughly the half of the value reported for the coarse-grained counterparts [21]. This illustrates the strong effect of grain refinement at the nanometer scale and the urgent need for a thorough revision of phase diagrams for nanostructured materials.

Another interesting result of the present experiments is the observed ability of the anatase phase to maintain its nanostructured character (average grain sizes: <10 nm) for temperatures as high as 460 °C at ambient pressure and for an extended temperature range (up to 600 °C) under moderate applied pressure (0.24 GPa). Under ambient pressure conditions, the faster growth of the anatase particles is triggered by the onset of the A → R transition (Fig. 2), however the titania specimens remain nanostructured up to temperatures as high as 850 °C. The observed anatase nanoparticle stabilization effect is consistent with the assumption that the more stable rutile phase nucleates on inner surfaces, thus giving rise to core–shell (rutile-coated anatase) nanoparticles. This assumption is also fully supported by the TG–DSC results (see also Section 3.3). Moreover, the presence of larger rutile nanoparticles already at the onset of the A → R phase transition (Figs. 1 and 6) would also be described in this way.

Both in situ X-ray diffraction and calorimetry experiments yielded results in good qualitative agreement, in spite of the fact that the thermal history of the samples investigated was different, resulting in somewhat different transition temperature values. The TG measurements offered additional insight into

the nature of the anatase grain-growth inhibition effect preceding the anatase-to-rutile transition, as well as into the evolution of solvent removal processes at lower temperatures.

The effect of applied pressure on the crystallization and sintering behavior of nanostructured titania was also investigated. We observed that even moderate pressures, as commonly encountered in pressure-assisted processing of ceramic materials, are able to induce a number of important effects. The onset of the A → R transition is detected at only 200 °C at 0.24 GPa instead of 460 °C under ambient pressure conditions. Also, the extent of the A → R phase transition (defined as the temperature range within which the anatase and rutile phases coexist) increases with almost 100 °C under applied pressure. Beyond the obvious technological relevance of these results for the further development of low-temperature low-pressure synthesis of nanostructured large-volume titania-based ceramics, we underline the importance of these observations for the full understanding of interface-controlled nucleation and growth processes. At present, the effect of applied pressure onto the stability, kinetics and sequence of phase transitions in nanophase materials may tentatively be understood in terms of pressure-induced changes of the surface tension and free energy, as well as atomic mobility and diffusion coefficients. A more detailed analysis of the high-pressure X-ray diffraction data [15] as well as further calorimetry experiments at ambient pressure are underway in order to resolve the individual contributions of the above mentioned factors to the overall stability behavior of these nanostructured materials.

Acknowledgements

We acknowledge the support of T. Traykova (Universität Rostock) with the sample preparation. We also thank C. Lathe, M. Knapp and C. Baehtz for their support provided at the MAX80 and B2 stations in HASYLAB. One of the authors (M.S.) gratefully acknowledges the financial support of the DFG Graduate College “Physics of Many-Particle Systems” (Universität Rostock). This work was supported by the IHP-Contract HPRI-CT-1999-00040/2001-00140 of the European Commission.

References

[1] H. Gleiter, Acta Mater. 48 (2000) 1–29.
[2] B. O’Regan, M. Grätzel, Nature 353 (1991) 737;
U. Bach, D. Lupo, P. Comte, J.E. Moser, F. Weissö, J. Salbeck, H. Spreitzer, M. Graetzel, Nature 395 (1998) 583.
[3] A. Fujishima, T.N. Rao, D.A. Tryk, J. Photochem. Photobiol. C: Photochem. Rev. 1 (2000) 1–21.
[4] H. Bach (Ed.), Thin Films on Glass, Schott Series on Glass and Glass Ceramics, Springer-Verlag, Berlin, 1997.
[5] H. Zhang, J.F. Banfield, J. Phys. Chem. B 104 (2000) 3481; H. Zhang, J.F. Banfield, J. Mater. Chem. 8 (1998) 2073.
[6] S.C. Liao, Y.J. Chen, W.E. Mayo, B.H. Kear, Nanostruct. Mater. 11 (1999) 553.
[7] S.C. Liao, J. Colaizzi, Y.J. Chen, B.H. Kear, W.E. Mayo, J. Am. Ceram. Soc. 83 (2000).
[8] S.C. Liao, K.D. Pae, W.E. Mayo, Nanostruct. Mater. 8 (1997) 645.
[9] S.C. Liao, K.P. Pae, W.E. Mayo, Mater. Sci. Eng. A 204 (1995) 152.
[10] S.C. Liao, K.P. Pae, W.E. Mayo, Nanostruct. Mater. 5 (1995) 319.
[11] PeakFit for Windows User’s Manual, SPSS Science, Inc., ISBN 1-56827-183-2.
[12] N.C. Halder, C.N.J. Wagner, Adv. X-ray Anal. 9 (1996) 91.
[13] D. Balzar, H. Ledbetter, J. Appl. Cryst. 26 (1993) 97.
[14] H.P. Klug, L.E. Alexander, X-ray Diffraction Procedures, Wiley, New York, 1974.
[15] R. Nicula, M. Stir, C. Schick, E. Burkel, in preparation.
[16] M. Stir, T. Traykova, R. Nicula, E. Burkel, C. Baehtz, M. Knapp, C. Lathe, Nuclear Instrum. Methods: Phys. B 199 (2003) 59.
[17] J.A. Nuth, Nature 329 (1987) 589.
[18] M.Y. Gamarnik, Nanostruct. Mater. 7 (1996) 651.
[19] R.C. Garvie, J. Phys. Chem. 82 (1978) 218.
[20] J.M. McHale, A. Auroux, A.J. Perrotta, A. Navrotsky, Science 277 (1997) 788.
[21] R.D. Shannon, J.A. Pask, J. Am. Ceram. Soc. 48 (1965) 391.
[22] W. Ma, Z. Lu, M. Zhang, Appl. Phys. A 66 (1998) 621.
[23] X.S. Ye, J. Sha, Z.K. Jiao, L.D. Zhang, Nanostruct. Mater. 8 (1997) 919.
[24] S.H. Tolbert, A.P. Alivisatos, Annu. Rev. Phys. Chem. 46 (1995) 595.